

Tilted anisotropic Dirac cones in quinoid-type graphene and α -(BEDT-TTF) $_2$ I $_3$

M.O. Goerbig, J.-N. Fuchs, G. Montambaux, and F. Piéchon

Laboratoire de Physique des Solides, CNRS UMR 8502, Univ. Paris-Sud, F-91405 Orsay cedex, France

We investigate a generalized two-dimensional Weyl Hamiltonian, which may describe the low-energy properties of mechanically deformed graphene and of the organic compound α -(BEDT-TTF) $_2$ I $_3$ under pressure. The associated dispersion has generically the form of tilted anisotropic Dirac cones. The tilt arises due to next-nearest-neighbor hopping when the Dirac points, where the valence band touches the conduction band, do not coincide with crystallographic high-symmetry points within the first Brillouin zone. Within a semiclassical treatment, we describe the formation of Landau levels in a strong magnetic field, the relativistic form of which is reminiscent to that of graphene, with a renormalized Fermi velocity due to the tilt of the Dirac cones. These relativistic Landau levels, experimentally accessible via spectroscopy or even a quantum Hall effect measurement, may be used as a direct experimental verification of Dirac cones in α -(BEDT-TTF) $_2$ I $_3$.

PACS numbers: 73.61.Wp, 73.61.Ph, 73.43.-f

I. INTRODUCTION

The discovery of a particular quantum Hall effect in graphene^{1,2} has shown that the low-energy electronic properties in this two-dimensional (2D) carbon crystal are described not in terms of a Schrödinger-type wave equation but by a relativistic Dirac equation.³ Due to a π -band, which shrinks at half-filling to two inequivalent points at the corners of the first Brillouin zone (BZ), the electronic energy dispersion is almost linear resulting in Dirac cones. This is reminiscent of the case of massless relativistic particles, where the speed of light c is replaced by a Fermi velocity v_F , which is roughly 300 times smaller than c .

Another material where Dirac cones are expected to occur is the organic 2D compound α -(BEDT-TTF) $_2$ I $_3$ under pressure.^{4,5,6} The relativistic behavior of the carriers may be at the origin⁴ of an experimentally observed T^2 dependence of the carrier density.^{7,8} Whereas in graphene, the Dirac cones at the corners of the first BZ are isotropic, they are situated within the first BZ in α -(BEDT-TTF) $_2$ I $_3$, strongly anisotropic, and *tilted* in the wave-vector energy space (\mathbf{k}, E) .^{4,5} The electronic properties are described by a generalized Weyl Hamiltonian with terms linear in the 2D wave vector \mathbf{k} . However, in contrast to graphene, there is yet no direct experimental evidence for the presence of Dirac cones in α -(BEDT-TTF) $_2$ I $_3$ or whether the system is simply a narrow-gap semiconductor.

In the present paper, we study the structure of the generalized Weyl Hamiltonian, which yields energy dispersions in form of tilted anisotropic Dirac cones. In the presence of a strong magnetic field, the dispersion is quantized in relativistic Landau levels (LLs), with the characteristic $\pm\sqrt{nB}$ behavior known from graphene. The tilt and the anisotropy of the Dirac cones give rise to a renormalization of the effective Fermi velocity and therefore of the typical LL spacing.

One example of a 2D system described by such generalized Weyl equation may be the above-mentioned or-

ganic material α -(BEDT-TTF) $_2$ I $_3$. We show, within an effective tight-binding model on an anisotropic triangular lattice with two atoms per unit cell,⁹ that the tilting of the Dirac cones is due to next-nearest-neighbor (*nnn*) hopping, which may be in α -(BEDT-TTF) $_2$ I $_3$ on the same order of magnitude as nearest-neighbor (*nn*) hopping.^{10,11} A necessary condition for *nnn* hopping to cause a tilt of the Dirac cones is that they are situated at points in the first BZ different from those of high crystallographic symmetry, such as its corners. Furthermore, we show that it may equally apply to graphene when the Dirac points, \mathbf{D} and \mathbf{D}' move away from the high-symmetry points \mathbf{K} and \mathbf{K}' at the corners of the first BZ. In this case the wave-vector expansion of the *nnn* term yields a linear contribution, whereas it is quadratic when the Dirac points coincide with the BZ corners \mathbf{K} and \mathbf{K}' . Such motion of the Dirac points may indeed be induced by a quinoid-type lattice distortion¹² of the graphene sheet. However, we show that the tilt of the Dirac cones is much less pronounced than in α -(BEDT-TTF) $_2$ I $_3$. Alternatively, this motion of Dirac points may be studied in cold atoms in an optical lattice where one may deform the honeycomb lattice and fine-tune the *nn* and *nnn* hopping parameters with the help of the laser intensities, wavelengths, and relative orientation.¹³

The paper is organized as follows. We start with a theoretical discussion of the generalized Weyl Hamiltonian in Sec. II. Sec. III is devoted to the LL formation in a strong magnetic field, for the case of tilted Dirac cones. Possible experimental realizations in distorted graphene and α -(BEDT-TTF) $_2$ I $_3$ are discussed in Sec. IV, which we conclude with an analysis of a possible quantum Hall effect in α -(BEDT-TTF) $_2$ I $_3$.

II. GENERALIZED WEYL HAMILTONIAN

We consider a model of two-spinor fermions restricted to a 2D space. Whereas the two-spinor form is in general dictated by relativistic invariance in two space dimensions, it naturally arises in the condensed matter

situation of a lattice with two inequivalent sites. The most general Hamiltonian linear in the 2D wave vector $\mathbf{k} = (k_x, k_y)$, is given by the “generalized Weyl Hamiltonian”,

$$H = \sum_{\mu=0,\dots,3} \mathbf{v}_\mu \cdot \mathbf{k} \sigma^\mu, \quad (1)$$

in terms of the velocities $\mathbf{v}_\mu = (v_\mu^x, v_\mu^y)$, and the 2×2 Pauli matrices $\sigma^0 \equiv \mathbb{1}, \vec{\sigma} = (\sigma^1, \sigma^2, \sigma^3)$. Here and in the following parts, we choose a unit system with $\hbar \equiv 1$. Both 2D space components of the velocities, $v_\mu^x = (v_0^x, \vec{v}^x) \equiv (v_0^x, v_1^x, v_2^x, v_3^x)$ and $v_\mu^y = (v_0^y, \vec{v}^y) \equiv (v_0^y, v_1^y, v_2^y, v_3^y)$, are in themselves vectors in the 4D spin space [the space of $SU(2)$ matrices] spanned by the Pauli matrices. The usual 2D Weyl Hamiltonian, which describes for instance low-energy massless electrons in graphene,³ is included in (1) if one considers $\mathbf{v}_0 = \mathbf{v}_4 = 0$, $\mathbf{v}_1 = (v_F, 0)$, and $\mathbf{v}_2 = (0, v_F)$, in terms of the Fermi velocity v_F .

Although, at first sight, the Weyl Hamiltonian is described by eight different parameters, given by the four two-component velocities \mathbf{v}_μ , it is indeed overspecified. In order to illustrate this point, we rewrite the Hamiltonian (1) in a different manner,

$$H = \mathbf{v}_0 \cdot \mathbf{k} \sigma^0 + (\vec{v}^x k_x + \vec{v}^y k_y) \cdot \vec{\sigma}. \quad (2)$$

One may get rid of two parameters ($\mathbf{v}_3 = 0$) by choosing the 3-quantization axis in the $SU(2)$ space perpendicular to the vectors \vec{v}^x and \vec{v}^y .

This point is indeed remarkable and needs to be discussed in the light of graphene physics. In this case, a constant σ^3 term breaks the inversion symmetry of the honeycomb lattice, e.g. due to a different on-site energy of the two triangular sublattices. Usually, this gives rise to a mass term and breaks the particle-hole symmetry. In the generalized Weyl Hamiltonian, this is not the case because the σ^3 term is linear in the wave vector and therefore does not affect the zero-energy state at $\mathbf{k} = 0$.

One may furthermore reduce the number of relevant model parameters by a simple rotation of the 2D frame of reference, accompanied by a unitary transformation in the $SU(2)$ space, which leaves the 3-quantization axis invariant. One, thus, obtains the “minimal” Weyl Hamiltonian

$$H = \mathbf{w}_0 \cdot \mathbf{q} \sigma^0 + w_x q_x \sigma^x + w_y q_y \sigma^y, \quad (3)$$

in terms of the four effective velocities $\mathbf{w}_0 = (w_{0x}, w_{0y})$, w_x and w_y . A detailed discussion of the involved transformations and a derivation of the exact expressions for the effective velocities may be found in the Appendix A.

The diagonalization of the minimal Weyl Hamiltonian yields the energy dispersions

$$\epsilon_\lambda(\mathbf{q}) = \mathbf{w}_0 \cdot \mathbf{q} + \lambda \sqrt{w_x^2 q_x^2 + w_y^2 q_y^2}, \quad (4)$$

where $\lambda = \pm$ plays the role of the band index.

For $w_x = w_y = v_F$ and $\mathbf{w}_0 = 0$, one obtains the isotropic model, which applies e.g. to the low-energy

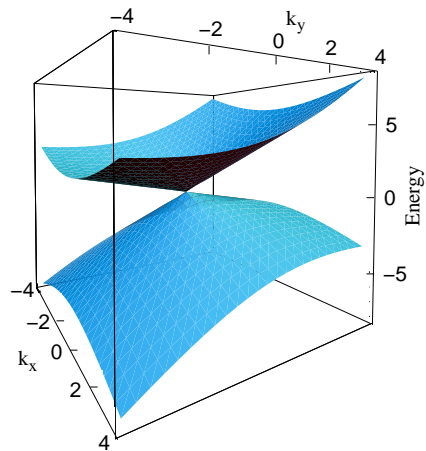


FIG. 1: Energy dispersion (4) for the special choice of $w_x = w_y = 1$, and $\mathbf{w}_0 = (0, 0.6)$, in natural units. The Dirac cone is tilted in the y -direction.

electronic properties in graphene: the Fermi velocities are the same in the x - and y -direction. The rotational symmetry is broken if $w_x \neq w_y$ (anisotropic model). Such case may be obtained e.g. if the graphene sheet is constrained by a uniaxial pressure, as is discussed in Sec. IV A. For $\mathbf{w}_0 \neq 0$, the Dirac cones are tilted away from the z -axis, as is shown in Fig. 1.

Notice that not all values of the tilt parameter \mathbf{w}_0 are indeed physical. In order to be able to associate $\lambda = +$ to a positive and $\lambda = -$ to a negative energy state, one obtains the condition

$$\left(\frac{w_{0x}}{w_x}\right)^2 + \left(\frac{w_{0y}}{w_y}\right)^2 < 1. \quad (5)$$

Unless this condition is satisfied, the iso-energetic lines are no longer ellipses but hyperbolas. Notice that, here, we aim to use the generalized Weyl Hamiltonian (1) and its resulting energy dispersion (4) to describe the electronic properties of particular 2D materials. Although it may be interesting to speculate about the resulting properties of a model that violates the condition (5), we are not aware of any physical example which might correspond to such a case.

In a 2D lattice system with valley degeneracy, a generalized Weyl Hamiltonian may describe the low-energy excitations in different valleys separately. In the remainder of this paper, we will in general only consider a single valley (and explicitly mention the inclusion of the twofold valley degeneracy when needed). Note also that we do not consider the true electron spin and do not include the corresponding twofold spin degeneracy.

In order to discuss the symmetry properties of the generalized Weyl Hamiltonian (3), it is convenient to introduce the unitary and Hermitian chirality operator

$$C = \frac{w_x q_x \sigma^x + w_y q_y \sigma^y}{\sqrt{w_x^2 q_x^2 + w_y^2 q_y^2}}, \quad (6)$$

which commutes naturally with the Hamiltonian. The associated eigenvalues are $\alpha = \pm 1$ and coincide with the band indices $\alpha = \lambda$. As exemplified in Sec. IV, this is generally not the case in a physical condensed-matter situation – the Weyl Hamiltonian corresponds to the effective model at Dirac points, where the conduction band touches the valence band; these Dirac points occur in pairs, at inequivalent points in the first BZ, which yields a twofold valley degeneracy. In this case, the effective model is rather given by ξH , where $\xi = \pm$ denotes the two valleys, and the relation between band index, chirality, and valley index is given by

$$\lambda = \xi\alpha. \quad (7)$$

In the present discussion, we may however identify the band index with the chirality, for simplicity.

The eigenstates of the chirality operator are

$$\Psi_\alpha = \frac{1}{\sqrt{2}} \begin{pmatrix} e^{-i\phi_{\mathbf{k}}} \\ \alpha \end{pmatrix}, \quad (8)$$

where $\tan \phi_{\mathbf{k}} \equiv w_y k_y / w_x k_x$. These eigenstates are also the natural eigenstates for the generalized Weyl Hamiltonian.

III. TILTED DIRAC CONES IN A MAGNETIC FIELD

We use the Peierls substitution to obtain the generalized Weyl Hamiltonian in a magnetic field

$$\mathbf{q} \rightarrow \mathbf{\Pi} = \mathbf{q} + e\mathbf{A}, \quad (9)$$

where \mathbf{A} is the vector potential that generates the (uniform) magnetic field $B\mathbf{e}_z = \nabla \times \mathbf{A}$ perpendicular to the 2D plane. With the help of the ladder operators

$$\begin{aligned} a &= \frac{l_B}{\sqrt{2w_x w_y}} (w_x \Pi_x - i w_y \Pi_y), \\ a^\dagger &= \frac{l_B}{\sqrt{2w_x w_y}} (w_x \Pi_x + i w_y \Pi_y), \end{aligned} \quad (10)$$

in terms of the magnetic length $l_B = 1/\sqrt{eB}$, one obtains the Hamiltonian

$$H_B = \frac{\sqrt{2w_x w_y}}{l_B} \begin{pmatrix} \frac{\tilde{w}_0}{2} (ae^{i\varphi} + a^\dagger e^{-i\varphi}) & a \\ a^\dagger & \frac{\tilde{w}_0}{2} (ae^{i\varphi} + a^\dagger e^{-i\varphi}) \end{pmatrix}. \quad (11)$$

where we have defined

$$\tilde{w}_0 e^{i\varphi} \equiv \frac{w_{0x}}{w_x} + i \frac{w_{0y}}{w_y},$$

in terms of the effective tilt parameter

$$\tilde{w}_0 \equiv \sqrt{\left(\frac{w_{0x}}{w_x}\right)^2 + \left(\frac{w_{0y}}{w_y}\right)^2}. \quad (12)$$

Instead of the full solution of the Hamiltonian (11), we consider the effect of the magnetic field in a semiclassical treatment. The Onsager relation¹⁴ states that the surface $S(\epsilon)$ enclosed by a trajectory of constant energy ϵ in reciprocal space is quantized as

$$S(\epsilon) l_B^2 = (2\pi)^2 \int_0^\epsilon d\epsilon' \rho(\epsilon') = 2\pi(n + \gamma),$$

where n is an integer denoting the energy level which coincides with the Landau level in the full quantum treatment. The additional contribution γ is related to a Berry phase acquired by an electron during its cyclotron orbit. Usually, one has $\gamma = 1/2$ except if there is an extra Berry phase of π , which in our case yields $\gamma = 0$, as in the case of graphene with no tilt.¹⁵ If one considers a density of states which scales as $\rho(\epsilon) \propto \epsilon^\alpha$, the energy levels thus scale as

$$\epsilon_n \sim [B(n + \gamma)]^{1/(1+\alpha)}, \quad (13)$$

in the large- n limit. In usual (non-relativistic) 2D electron systems, one finds a constant density of states, i.e. $\alpha = 0$, and $\gamma = 1/2$. The scaling of the conventional Landau levels is therefore $\epsilon_n \propto B(n + 1/2)$. In the relativistic case of electrons in graphene, the density of states vanishes linearly at the Dirac points, and one therefore obtains $\epsilon_n \propto \sqrt{Bn}$ because $\alpha = 1$ and $\gamma = 0$. The relation (13) has been generalized to the case of a spatially anisotropic density of states by Dietl *et al.*¹⁶

From the scaling argument (13) in the large- n limit, one may notice that the B -field scaling of the levels must be the same as the n scaling. Furthermore, one sees from the quantum Hamiltonian (11) that the energy must scale as $1/l_B \propto \sqrt{B}$. Therefore, the energy levels must obey, in the large- n limit, the equation

$$\epsilon_{\lambda,n} \simeq \lambda \sqrt{2} \frac{v_F^*}{l_B} \sqrt{n}, \quad (14)$$

as in the case of the Weyl equation for massless charged particles, such as in graphene, apart from a renormalization of the Fermi velocity.

The renormalization of the Fermi velocity may be obtained from the calculation of the density of states. The total number of states below a given energy ϵ within the positive energy cone is given by

$$\begin{aligned} N_+(\epsilon) &= \frac{1}{(2\pi)^2 w_x w_y} \int_{\epsilon_+(\tilde{q}) \leq \epsilon} d\tilde{q}_x d\tilde{q}_y \\ &= \frac{1}{2\pi v_F^{*2}} \frac{\epsilon^2}{2}, \end{aligned}$$

where we have defined $\tilde{q}_{x/y} \equiv w_{x/y} q_{x/y}$, and the renormalized Fermi velocity is written in integral form,

$$\frac{1}{v_F^{*2}} = \frac{1}{w_x w_y} \int_0^{2\pi} \frac{d\phi}{2\pi} \frac{1}{(1 + \tilde{w}_0 \cos \phi)^2}. \quad (15)$$

in terms of the effective tilt parameter (12). One notices from Eq. (15) that if the condition (5), $|\tilde{w}_0|^2 < 1$, is

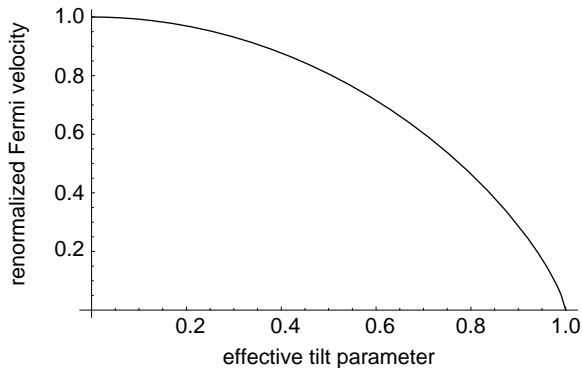


FIG. 2: Renormalized Fermi velocity $v_F^*/\sqrt{w_x w_y}$ as a function of the effective tilt parameter $\tilde{w}_0 \equiv \sqrt{(w_{0x}/w_x)^2 + (w_{0y}/w_y)^2}$. The Fermi velocity vanishes for $\tilde{w} = 1$, where the orbits change from ellipses to hyperbolas.

not satisfied, the expression under the integral diverges because the denominator may become zero. This result is not surprising because the Onsager quantization relation, which yields the energy levels (14) is only valid for closed orbits, given e.g. by the elliptic isoenergetic lines. As already mentioned, the orbits for $|\tilde{w}_0| \geq 1$ are open hyperbolas, and the expression (14) is no longer valid.

The density of states is obtained by differentiation of the number of states,

$$\rho(\epsilon) = \frac{|\epsilon|}{2\pi v_F^{*2}}, \quad (16)$$

which is the concise expression for both the positive and negative parts of the tilted Dirac cones.

The \sqrt{nB} behavior of Eq. (14) is, strictly speaking, valid only in the large- n limit. However, usually it yields extremely good estimates for the levels down to values as small as $n = 1$. Special care is needed for the discussion of the $n = 0$ level, which requires a quantum treatment of the Hamiltonian (11). In the following, we discuss the fate of the zero-energy Landau level.

The behavior of this level may be understood with the help of the quantum treatment of the Hamiltonian for $\mathbf{w}_0 = 0$. In this case, the expression (14) is exact with $v_F^* = \sqrt{w_x w_y}$, which is also the $\mathbf{w}_0 = 0$ -limit of the expression (15). There exists thus a zero-energy level for $n = 0$, which has the same degeneracy, N_B as all other levels (λ, n), in terms of the number of flux quanta $N_B = AB/(h/e)$ threading the total surface A .

For non-zero values of \mathbf{w}_0 , the Hamiltonian (11) may not be diagonalized by a simple canonical transformation. However, the Hamiltonian (11) is transformed as $H_B \rightarrow -H_B$ under space inversion, $\mathbf{r} \rightarrow -\mathbf{r}$, as shown in the Appendix B. This implies that the energy spectrum is symmetric around zero energy (see Appendix B). Therefore, starting from $\mathbf{w}_0 = 0$ and adiabatically turning on $\mathbf{w}_0 \neq 0$, there are only two possibilities for the evolution of the zero-energy level: (i) either it remains at

zero energy or (ii) it splits into (at least) two sublevels 0^+ and 0^- , which are symmetric around zero energy. However, splitting of the zero-energy level into sublevels can be excluded on account of the degeneracy of this level. Indeed, when $\mathbf{w}_0 = 0$, the exact degeneracy of the zero energy ($n = 0$) Landau level is given by N_B (remember that we only consider a single valley here). When $\mathbf{w}_0 \neq 0$, it can, therefore, not split since this would indeed lead to an unphysical doubling of the number of quantum states because each level, 0^+ and 0^- , would have to be N_B times degenerate. Therefore, for all magnetic field strength, there exist a zero-energy Landau level. The explicit expressions for the zero-energy wave functions may be found in the Appendix C. Notice, that this is consistent with the semiclassical spectrum with $\gamma = 0$.

In the above treatment, we only considered a single valley. We note however that the magnetic field might introduce a coupling between the two valleys. In such a case, we do not exclude a parity anomaly which consists of a different behavior of the $n = 0$ level at the two inequivalent Dirac points at non-zero wave vectors in a lattice model. In this case, space inversion would involve the low-energy Hamiltonians at both Dirac points, and the spectrum is only symmetric around zero energy if one accounts for both valleys. The parity anomaly is, however, expected to play no physical role in the continuum limit with $a/l_B \rightarrow 0$, where a is the lattice spacing.

In conclusion, we have obtained the semiclassical spectrum of Landau levels [see Eqs (14)-(12)], valid when $n \gg 1$ and checked that the zero energy level ($n = 0$) indeed exists in a full quantum treatment. Based on this two calculations, we expect the semiclassical spectrum to be a very good approximation to the true quantum spectrum of Landau levels, for all n . This is one of the main result of the present paper.

IV. PHYSICAL EXAMPLES OF TILTED DIRAC CONES

After this rather technical discussion of the generalized Weyl Hamiltonian and tilted Dirac cones, we discuss, here, two physical systems which may display these properties. We find that whereas the tilt of the Dirac cones is well pronounced and thus strongly affects the Landau level quantization in α -(BEDT-TTF) $_2$ I $_3$, it is much more difficult to induce a tilt in graphene via a lattice deformation. However, a quinoid-type lattice deformation is also discussed for pedagogical reasons because the general physical origin of tilted Dirac cones becomes transparent.

A. Quinoid-type graphene under uniaxial strain

As a first example, we consider a graphene sheet which is deformed in one of its principle symmetry axes. This particular deformation results in a quinoid variety of the

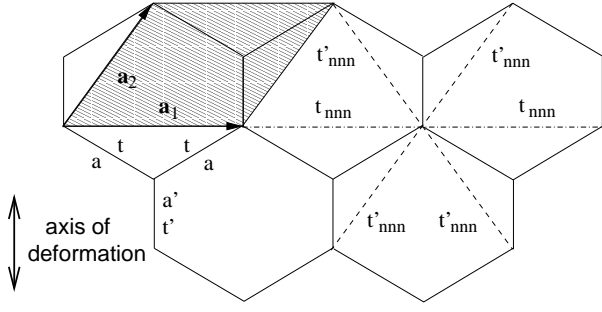


FIG. 3: Quinoid-type deformation of the honeycomb lattice – the bonds parallel to the deformation axis (double arrow) are modified. The shaded region indicates the unit cell of the oblique lattice, spanned by the lattice vectors \mathbf{a}_1 and \mathbf{a}_2 . Dashed and dashed-dotted lines indicate next-nearest neighbors, with characteristic hopping integrals t_{nnn} and t'_{nnn} , respectively, which are different due to the lattice deformation.

honeycomb lattice.¹⁷ We treat its electronic properties within the tight-binding approximation. Starting from the graphene honeycomb lattice, with equal bond length $a \simeq 0.14$ nm and equal nn hopping energy $t \simeq 3$ eV, the bond length and hopping energy are modified in the deformation axis (see Fig. 3),

$$a \rightarrow a' = a + \delta a \quad \text{and} \quad t \rightarrow t' = t + \frac{\partial t}{\partial a} \delta a,$$

and kept unchanged otherwise. We call $\varepsilon = \delta a/a$ the relative strain. Here, we consider a moderate deformation, $|\varepsilon| \ll 1$, such that one may linearize the hopping energy around its nondeformed value t , and $\partial t/\partial a \simeq -5$ eV/Å.^{17,18} This value agrees with an evaluation based on Harrison's law¹⁹ according to which $t = C\hbar^2/ma^2$, where C is a numerical prefactor of order one. Derivation with respect to a yields

$$\frac{\partial t}{\partial a} = -\frac{2t}{a} \sim -4.3 \text{ eV/\AA}. \quad (17)$$

For simplicity and as a first approximation, one may keep the bond angles fixed at $2\pi/3$. The underlying Bravais lattice is no longer triangular but oblique with the basis vectors

$$\mathbf{a}_1 = \sqrt{3}a\mathbf{e}_x \quad \text{and} \quad \mathbf{a}_2 = \frac{\sqrt{3}}{2}a\mathbf{e}_x + \left(\frac{3}{2}a + \delta a\right)\mathbf{e}_y,$$

and the reciprocal lattice is spanned by the vectors

$$\mathbf{a}_1^* = 2\pi \left(\frac{\mathbf{e}_x}{\sqrt{3}a} - \frac{\mathbf{e}_y}{3a + 2\delta a} \right) \quad \text{and} \quad \mathbf{a}_2^* = \frac{4\pi\mathbf{e}_y}{3a + 2\delta a}.$$

Furthermore, we take into account nnn hopping, with a characteristic energy of²⁰ $t_{nnn} \simeq 0.1t$ in the undeformed horizontal axes. The deformation yields, in the same manner as for the nn hopping energies, different hopping energies for the other directions (see Fig. 3),

$$t_{nnn} \rightarrow t'_{nnn} = t_{nnn} + \frac{\partial t_{nnn}}{\partial a} \delta a.$$

The tight-binding model may be described by the Hamiltonian

$$H = \sum_{\mathbf{q}} (a_{\mathbf{q}}^\dagger, b_{\mathbf{q}}^\dagger) \mathcal{H}_{\mathbf{q}} \begin{pmatrix} a_{\mathbf{q}} \\ b_{\mathbf{q}} \end{pmatrix} \quad (18)$$

in reciprocal space, where $a_{\mathbf{q}}^{(\dagger)}$ and $b_{\mathbf{q}}^{(\dagger)}$ are the Fourier components of the annihilation (creation) operators on the A and B sublattices, respectively. The Hamiltonian 2×2 matrix

$$\mathcal{H}_{\mathbf{q}} = \begin{pmatrix} h'(\mathbf{q}) & h^*(\mathbf{q}) \\ h(\mathbf{q}) & h'(\mathbf{q}) \end{pmatrix}$$

is given in terms of the elements

$$\begin{aligned} h(\mathbf{q}) &= -t \left[e^{i(q_y + \sqrt{3}q_x)a/2} + e^{i(q_y - \sqrt{3}q_x)a/2} \right] \\ &\quad - t' e^{-iq_y(a + \delta a)} \\ &= -2t \cos \frac{q_y a}{2} \cos \frac{\sqrt{3}q_x a}{2} - t' \cos [q_y(a + \delta a)] \\ &\quad - i \left\{ 2t \sin \frac{q_y a}{2} \cos \frac{\sqrt{3}q_x a}{2} - t' \sin [q_y(a + \delta a)] \right\} \end{aligned} \quad (19)$$

and

$$\begin{aligned} h'(\mathbf{q}) &= 2t_{nnn} \cos \sqrt{3}q_x a \\ &\quad + 2t'_{nnn} \left\{ \cos \left[\frac{\sqrt{3}q_x a}{2} + q_y \left(\frac{3}{2}a + \delta a \right) \right] \right. \\ &\quad \left. + \cos \left[-\frac{\sqrt{3}q_x a}{2} + q_y \left(\frac{3}{2}a + \delta a \right) \right] \right\}, \end{aligned} \quad (20)$$

The energy dispersion is obtained from the eigenvalues of $\mathcal{H}_{\mathbf{q}}$,

$$\epsilon_{\lambda}(\mathbf{q}) = h'(\mathbf{q}) + \lambda |h(\mathbf{q})| \quad (21)$$

and is plotted in Fig. 4 for a deformation of $\delta a/a = 0.4$. The two bands, $\lambda = +$ and $\lambda = -$, touch each other at the Dirac points \mathbf{q}^D , which are obtained from the condition $h(\mathbf{q}^D) = 0$,¹⁶

$$q_y^D = 0 \quad \text{and} \quad q_x^D a = \xi \frac{2}{\sqrt{3}} \arccos \left(-\frac{t'}{2t} \right), \quad (22)$$

where $\xi = \pm$ denotes the two inequivalent Dirac points D and D' , respectively. In the absence of any distortion, the Dirac points D and D' coincide with the crystallographic points K and K' , respectively, at the corners of the first BZ. The distortion makes both pairs of points move in the same direction due to the negative value of $\partial t/\partial a$. However, unless the parameters are fine-tuned, this motion is different, and the two pairs of points no longer coincide.²¹

The low-energy properties of electrons in a quinoid-type distorted graphene sheet are described by the linearized model around the Dirac points, which is exactly of the form (3) of the Weyl Hamiltonian,

$$H^{\xi} = \xi (\mathbf{w}_0 \cdot \mathbf{k} \sigma^0 + w_x k_x \sigma^x + w_y k_y \sigma^y), \quad (23)$$

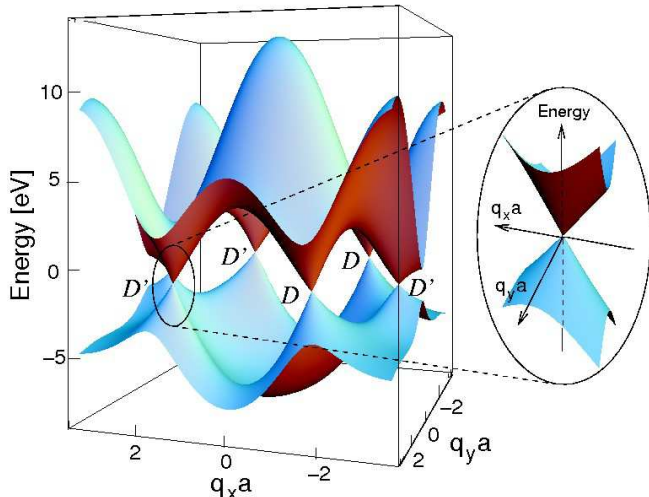


FIG. 4: Energy dispersion of the quinoid-type deformed the honeycomb lattice, for a lattice distortion of $\delta a/a = 0.4$, with $t = 3$ eV, $t_{nnn}/t = 0.1$, $\partial t/\partial a = -5$ eV/Å, and $\partial t_{nnn}/\partial a = -0.7$ eV/Å. The inset shows a zoom on one of the Dirac points, D' .

with the effective velocities

$$\begin{aligned} w_x &= \sqrt{3}ta \sin \theta \\ w_y &= \frac{3}{2}t'a \left(1 + \frac{2\delta a}{3a}\right) \\ w_{0x} &= 2\sqrt{3}(t_{nnn}a \sin 2\theta + t'_{nnn}a \sin \theta) \\ w_{0y} &= 0, \end{aligned} \quad (24)$$

where we have defined $\theta \equiv \arccos(-t'/2t)$. The corresponding energy dispersion is independent of ξ , which is at the origin of the twofold valley degeneracy. In order to obtain the concise form of Eq. (23), we have chosen the spinor representation (ψ_A, ψ_B) at the $\xi = +$ Dirac point and (ψ_B, ψ_A) for $\xi = -$, i.e. interchanged the sublattice components at D' . As mentioned in Sed. II, the relation between the band index λ , chirality α , and valley index ξ is given by Eq. (7), $\lambda = \xi\alpha$, due to the global sign ξ in the Hamiltonian (23). The constant term $h'(\mathbf{q} = \xi\mathbf{q}^D)\mathbb{1}$ has been absorbed in a renormalization of the chemical potential, the position of which is determined by the electronic half-filling of the graphene sheet.

One notices from the Eqs. (24) that the quinoid-type distortion yields an anisotropy in the Fermi velocities, $w_x \neq w_y$, and that the Dirac cones are tilted due to $w_{0x} \neq 0$. The isotropic graphene model is retrieved at $\delta a = 0$ – one has then $w_x = w_y = v_F = 3ta/2 \simeq 6.3$ eVÅ and $w_{0x} = w_{0y} = 0$ because $t = t'$, $t_{nnn} = t'_{nnn}$, and $\sin \theta = \sqrt{3}/2 = -\sin 2\theta$, in the undeformed case. Without deformation, nnn hopping therefore does not affect the energy dispersion at linear order, but only at second order. This is due to the fact that the Dirac points are then situated at the high-symmetry crystallographic points K and K' . Indeed, this yields a

parabolic correction, which breaks the original electron-hole symmetry.^{3,22}

To summarize, in order to obtain tilted Dirac cones in graphene, two ingredients are required: (i) nnn hopping, which generates the diagonal components $h'(\mathbf{q})$ in the Hamiltonian (18); and (ii) for a linear contribution arising from this term, the Dirac points D and D' need to be shifted away from the high-symmetry points K and K' . This shift may be obtained by constraining the graphene sheet into such a quinoid type.

In the presence of a magnetic field, the LL spacing is affected by the deformation because the Fermi velocity is renormalized according to Eq. (15),

$$v_F^* \simeq \sqrt{w_x w_y} \left(1 - \frac{3}{4}\tilde{w}_0^2\right), \quad (25)$$

for small values of the effective tilt parameter \tilde{w}_0 . It may be evaluated from the model parameters,

$$\begin{aligned} \tilde{w}_0 &= 2 \left(\frac{t_{nnn}}{t} \frac{\sin 2\theta}{\sin \theta} + \frac{t'_{nnn}}{t} \right) \\ &\simeq \frac{2}{t^2} (tt'_{nnn} - t't_{nnn}). \end{aligned} \quad (26)$$

In order to estimate t'_{nnn} , we use the “atomic orbitals overlap law” familiar in the context of the extended Hückel model,²³

$$t_{nnn}(b, a) \approx t(a)e^{-(b-a)/d(a)}$$

where a is the nn distance, b is the nnn distance, and $d \approx a/3.5 \approx 0.4$ Å is a characteristic distance related to the overlap of atomic orbitals. In the undeformed graphene $b = a\sqrt{3}$, whereas in the quinoid type graphene $b' = b(1 + \varepsilon/2)$ and $a' = a(1 + \varepsilon)$. This gives $t'_{nnn} = t_{nnn}(1 - 2\varepsilon + b\varepsilon/2d)$ and $t' = t(1 - 2\varepsilon)$. Therefore, the effective tilt parameter is given by

$$\tilde{w}_0 \approx \frac{b}{d} \frac{t_{nnn}}{t} \varepsilon \approx 0.6\varepsilon.$$

As the correction to the Fermi velocity appears as $1 - 3\tilde{w}_0^2/4$ [see Eq. (25)], this effect remains extremely small, and the tilt affects the LL spacing in a negligible manner.

The main contribution to the renormalized Fermi velocity therefore arises not from the tilt of the Dirac cones (effect of order ε^2), but from the anisotropy in the Fermi velocities (effect of order ε), and one finds

$$v_F^* \simeq v_F \left[1 + \frac{1}{3} \left(\frac{\partial t}{\partial a} \frac{\delta a}{t} + \frac{\delta a}{a} \right) \right] \simeq v_F \left(1 - \frac{\varepsilon}{3} \right), \quad (27)$$

which may yield an experimentally observable effect in the percent range for a strain of $\varepsilon \sim 10\%$.

From an experimental point of view, such quinoid-type deformation may be realized if one uses a piezoelectric substrate, on which the graphene sheet is posed, instead of the most commonly used SiO₂. Another possibility would be to use a mechanical deformation

of the underlying substrate. Such bending has been exploited e.g. to investigate carbon nanotubes under strain.²⁴ More recently, graphene on polydimethylsiloxane (PDMS) has been put under uniaxial strain by bending of the PDMS.²⁵ The elastic regime in graphene requires that the strain is smaller than 10% and the rupture occurs around 20%. Therefore an upper bound for ε is certainly 10%.

B. Organic 2D compounds

Another example of a 2D metal, where tilted Dirac cones may occur, is the layered organic compound α -(BEDT-TTF)₂I₃ under (uniaxial) pressure.^{4,5,6} Each layer may be described by an oblique lattice with four sites per unit cell, and the electronic filling is 3/4. In the vicinity of the Fermi energy, only two out of the four bands are relevant for the low-energy electronic properties. It has indeed been shown that the band structure may be modeled with great precision within a tight-binding model on a half-filled anisotropic triangular lattice with nn and nnn hopping, where each site corresponds to a dimer.⁹ This is a natural assumption for κ - and λ -(BEDT-TTF)₂I₃, where there exists one hopping energy which is largely enhanced with respect to the others. In contrast to these compounds, the assumption may seem hazardous at first sight in the case of α -(BEDT-TTF)₂I₃, where there is no such clearly enhanced hopping energy, such that the dimerization is expected to be rather weak. Furthermore, these organic materials exhibit strong electronic correlations, and a tight-binding calculation for quasi-free electrons sweeps a lot of interesting physics under the carpet. However, the high-pressure limit corresponds to a regime where the electrons are less strongly correlated and where interaction effects may be taken into account via renormalized effective hopping parameters.⁵

The tight-binding model on the anisotropic triangular lattice is depicted in Fig. 5. The nn are situated at the vectors $\pm\mathbf{a}_1$ and $\pm\mathbf{a}_2$, with

$$\boldsymbol{\delta}_1 = \frac{1}{2}(\mathbf{e}_x + \mathbf{e}_y) \quad \text{and} \quad \boldsymbol{\delta}_2 = \frac{1}{2}(\mathbf{e}_x - \mathbf{e}_y),$$

which connect sites on the different sublattices, A and B and the vectors

$$\mathbf{a}_1 = \boldsymbol{\delta}_1 + \boldsymbol{\delta}_2 = \mathbf{e}_x \quad \text{and} \quad \mathbf{a}_2 = \boldsymbol{\delta}_1 - \boldsymbol{\delta}_2 = \mathbf{e}_y$$

span the underlying Bravais lattice, which is chosen to be a square lattice, for simplicity. Notice that the lattice may also be viewed as an anisotropic 2D NaCl lattice (two inequivalent interpenetrating square lattices). The bond length is set to unity, $a \equiv 1$. The nn hopping energies are t_1 and t'_1 in the directions $\pm\mathbf{a}_1$, and t_2 and t'_2 in the directions $\mp\mathbf{a}_2$, respectively. The nnn hopping energy is t_{nnn} .

The effective tight-binding model may be written in the same manner (18) as for the case of quinoid-type

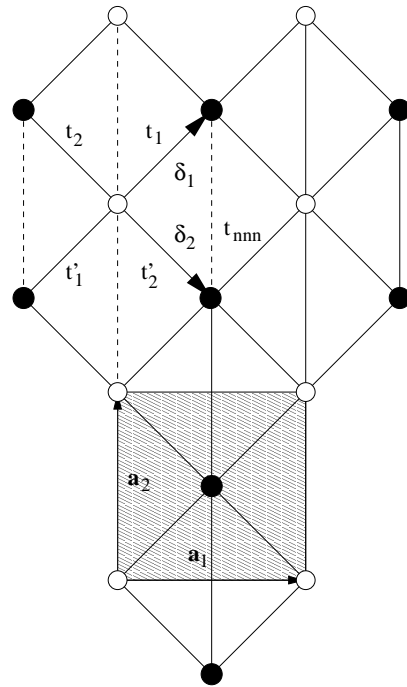


FIG. 5: Anisotropic triangular lattice model, with four different nn hopping energies, t_1 , t'_1 , t_2 , and t'_2 and the nnn hopping energy t_{nnn} . The unit cell with two inequivalent sites is represented by the shaded region. The sites of the A and B sublattices are depicted by the filled and open circles, respectively.

graphene, with the matrix elements

$$h(\mathbf{q}) = 2 \left[(t_1 + t'_1) \cos \frac{q_x + q_y}{2} + (t_2 + t'_2) \cos \frac{q_x - q_y}{2} \right] + 2i \left[(t_1 - t'_1) \sin \frac{q_x + q_y}{2} + (t_2 - t'_2) \sin \frac{q_x - q_y}{2} \right]$$

and

$$h'(\mathbf{q}) = 2t_{nnn} \cos q_y.$$

The energy dispersion is obtained from Eq. (21), and the position of the Dirac points is calculated from

$$\tan^2 \frac{q_x^D}{2} = -\frac{(t'_1 + t_2)^2 - (t_1 + t'_2)^2}{(t'_1 - t_2)^2 - (t_1 - t'_2)^2}$$

$$\tan^2 \frac{q_y^D}{2} = -\frac{(t'_1 + t'_2)^2 - (t_1 + t_2)^2}{(t'_1 - t'_2)^2 - (t_1 - t_2)^2}.$$

One may directly see that the r.h.s of both equations must be positive in order to have a pair of Dirac points (\mathbf{q}^D and $-\mathbf{q}^D$) within the first BZ, $-\pi/2 < q_x, q_y \leq \pi/2$.

An expansion around the Dirac points yields the generalized Weyl Hamiltonian (1),

$$H^\xi = \xi \sum_{\mu=0}^2 \mathbf{v}_\mu \cdot \mathbf{k} \sigma^\mu,$$

in terms of the velocities

$$\begin{aligned}
v_{0x} &= 0, & v_{0y} &= -2t_{nnn} \sin q_y^D, \\
v_1^x &= (t'_1 + t_1) \sin \frac{q_x^D + q_y^D}{2} + (t'_2 + t_2) \sin \frac{q_x^D - q_y^D}{2}, \\
v_1^y &= (t'_1 + t_1) \sin \frac{q_x^D + q_y^D}{2} - (t'_2 + t_2) \sin \frac{q_x^D - q_y^D}{2}, \\
v_2^x &= (t'_1 - t_1) \cos \frac{q_x^D + q_y^D}{2} + (t'_2 - t_2) \cos \frac{q_x^D - q_y^D}{2}, \\
v_2^y &= (t'_1 - t_1) \cos \frac{q_x^D + q_y^D}{2} - (t'_2 - t_2) \cos \frac{q_x^D - q_y^D}{2}.
\end{aligned} \tag{28}$$

Here, we have used the same spinor representation as for quinoid-type graphene, i.e. we have interchanged the sublattice components when changing the valley. One notices that the Dirac cones are tilted only if the Dirac points are not situated at the border of the first BZ, $q_y^D = \pi/2$. This corresponds to the high-symmetry crystallographic points in graphene, and nnn hopping affects the effective model again only at second order in the expansion around the Dirac points.

The experimental evidence for (tilted) Dirac cones in α -(BEDT-TTF) $_2$ I $_3$ compounds under pressure is yet rather weak. Whereas at ambient pressure, the material is an insulator due to charge ordering, temperature-dependent transport measurements under high hydrostatic pressure have revealed a T^2 dependence of the carrier density below 50 K,^{7,8} as one would expect for relativistic electrons with a linear dispersion relation.^{3,4} It is, however, not clear whether the compound has, under these circumstances, a truly vanishing gap as for massless relativistic electrons or whether a tiny gap persists. Furthermore the T^2 dependence of the carrier density is accompanied by a temperature-dependent mobility, which results in an essentially constant conductivity over a large temperature range.⁸

A more direct evidence for the relevance of Dirac cones in α -(BEDT-TTF) $_2$ I $_3$ would be a measurement of the characteristic properties of relativistic quantum Hall physics, as in the case of graphene.^{1,2,3} The following final part of this paper is devoted to the discussion of possible quantum Hall physics in α -(BEDT-TTF) $_2$ I $_3$.

Possible quantum Hall effect in α -(BEDT-TTF) $_2$ I $_3$

Although it is a delicate issue to yield energy values for the hopping parameters t_1, t'_1, t_2, t'_2 and t_{nnn} from the overlap integrals in α -(BEDT-TTF) $_2$ I $_3$,^{10,11} we expect that the good agreement between band-structure calculations in the full model with four sites per unit cell and the anisotropic triangular lattice model⁹ yields the correct orders of magnitude for the effective velocities (28). Using the prescription proposed by Hotta⁹ and the overlap integrals calculated by Mori *et al.*,¹⁰ we may estimate $t_1 = 36$ meV, $t'_1 = -86$ meV, $t_2 = -24$ meV, $t'_2 = -77$

meV, and $t_{nnn} = -60$ meV. These values yield a pair of Dirac points at \mathbf{q}^D and $-\mathbf{q}^D$, with $\mathbf{q}^D = (2.52, -3.08)$, in units of the inverse lattice constant, which is on the order of 10 \AA^{-1} .^{10,11,26} With the help of Eqs. (28), one thus obtains the effective velocities $v_1^x = -0.035 \text{ eV\AA}$, $v_1^y = 0.315 \text{ eV\AA}$, $v_2^x = -0.222 \text{ eV\AA}$, $v_2^y = -2.121 \text{ eV\AA}$, $v_{0x} = 0$, and $v_{0y} = 0.074 \text{ eV\AA}$. One notices a variation by almost two orders of magnitude, and one may therefore expect rather large anisotropies.

The effective velocities in the minimal model are calculated with the help of Eqs. (A3), and one finds a rotation angle of $\theta = 0.102$ and the velocities $w_x = 2.14 \text{ eV\AA}$, $w_y = 0.22 \text{ eV\AA}$, $w_{0x} = -0.0075 \text{ eV\AA}$, and $w_{0y} = 0.736 \text{ eV\AA}$. The average Fermi velocity is therefore $\sqrt{w_x w_y} = 0.69 \text{ eV\AA}$, which is roughly one order of magnitude smaller than that in graphene. The tilt parameter (12) is

$$\tilde{w}_0 = 0.33$$

and thus much larger than in the case of a quinoid-type deformation of a graphene sheet. The tilt therefore leads to a reduction of the average Fermi velocity, and one finds from Eq. (25) a renormalized velocity of

$$v_F^* \simeq 0.92 \sqrt{w_x w_y} \simeq 0.63 \text{ eV\AA}.$$

The renormalized Fermi velocity allows one to extract the typical energy scale for the Landau levels in α -(BEDT-TTF) $_2$ I $_3$, and one finds from Eq. (14) $\epsilon_{\lambda,n} = \lambda \omega_C^* \sqrt{n}$, with a characteristic ‘‘cyclotron’’ frequency of

$$\omega_C^* = \sqrt{2} \frac{v_F^*}{l_B} \simeq 3.4 \sqrt{B[T]} \text{ meV}, \tag{29}$$

which is, due to the smaller Fermi velocity, roughly one order of magnitude smaller than that in graphene. However, this energy scale is comparable to the cyclotron frequency in GaAs heterostructures ($\omega_C \simeq 1.6B[T]$ meV), which are most commonly used in the study of quantum Hall physics.²⁷ One may therefore expect that a relativistic quantum Hall effect^{1,2} could principally also occur in α -(BEDT-TTF) $_2$ I $_3$ if disorder does not prevent LL formation.

Experimentally, thin (BEDT-TTF) $_2$ I $_3$ films have already been synthesized.²⁸ Alternatively, one may hope that the exfoliation technique,²⁹ which has proven to be particularly successful in the fabrication of single-layer graphene sheets, also yields reasonably thin α -(BEDT-TTF) $_2$ I $_3$ samples. However, (BEDT-TTF) $_2$ I $_3$ crystals are generally of lower mechanical stability than carbon crystals, due to the relatively large lattice constants and the reduced binding energies.

Apart from a direct measurement of a quantum Hall effect in α -(BEDT-TTF) $_2$ I $_3$ compounds, one may probe the system via transmission spectroscopy in a magnetic field. This would allow for a direct measurement of the cyclotron frequency and for a check of the relativistic character of electrons in α -(BEDT-TTF) $_2$ I $_3$. Transmission spectroscopy has indeed been successfully applied to epitaxial³⁰ and exfoliated³¹ graphene and yields

a $\sqrt{B}(\sqrt{n+1} \pm \sqrt{n})$ scaling of the transmission lines, as expected for the relativistic quantum Hall effect in graphene.

V. CONCLUSIONS

In conclusion, we have investigated tilted Dirac cones in deformed graphene and the organic 2D material α -(BEDT-TTF)₂I₃. The low-energy electronic properties are described by a generalized Weyl Hamiltonian, which may in both physical systems be derived from a tight-binding model on a lattice with two inequivalent sites. Whereas the presence of pairs of Dirac points is due to nn hopping, which couples neighboring sites on inequivalent sublattices, the tilt of the Dirac cones arises from nnn hopping if the Dirac points are shifted away from the points of high crystallographic symmetry in the first Brillouin zone.

In the presence of a strong magnetic field, a semi-classical analysis yields the same structure of relativistic LLs as in non-deformed graphene, but with a renormalized effective Fermi velocity due to the tilt and the anisotropy of the Dirac cones. Whereas this effect is expected to be small in a quinoid-type deformation of the graphene, our estimates for the effective velocities for α -(BEDT-TTF)₂I₃ indicate that the tilt yields a significant reduction of the effective Fermi velocity, which determines the LL spacing. The largest spacing of the $0 \rightarrow +1$ and $-1 \rightarrow 0$ LL transitions is on the order of $3.4\sqrt{B[T]}$ meV, which is on the order of the (equidistant) LL spacing in GaAs heterostructures most commonly used in quantum Hall effect measurements. Such measurements in α -(BEDT-TTF)₂I₃, as well as LL spectroscopy, may be a possible experimental verification of the yet weakly corroborated presence of Dirac cones in α -(BEDT-TTF)₂I₃.

Acknowledgments

We acknowledge fruitful discussions with H el ene Bouchiat, Natasha Kirova, Claude Pasquier, Jean-Paul

Pouget, and Yoshikazu Suzumura. This work is partially supported by the Agence Nationale de la Recherche under Grant No. ANR-06-NANO-019-03.

APPENDIX A: DERIVATION OF THE MINIMAL WEYL HAMILTONIAN

In order to reduce the number of effective parameters in the Weyl Hamiltonian (2), one rotates the 2D reference system in the physical space,

$$\begin{aligned} k_x &= \cos \vartheta q_x + \sin \vartheta q_y \\ k_y &= -\sin \vartheta q_x + \cos \vartheta q_y, \end{aligned}$$

accompanied by a unitary transformation in the SU(2) space,

$$U(\theta) = \cos \frac{\theta}{2} \mathbb{1} + i \sin \frac{\theta}{2} \sigma^z,$$

which leaves the 3-quantization axis invariant and describes a rotation in the xy -plane in the SU(2) spin space,

$$\sigma^1 = \cos \theta \sigma^x + \sin \theta \sigma^y \quad (\text{A1})$$

$$\sigma^2 = -\sin \theta \sigma^x + \cos \theta \sigma^y. \quad (\text{A2})$$

If one chooses

$$\tan \theta = \frac{v_1^x \sin \vartheta + v_1^y \cos \vartheta}{v_2^x \sin \vartheta + v_2^y \cos \vartheta}$$

and

$$\begin{aligned} \tan 2\vartheta &= -\frac{2(v_1^x v_1^y + v_2^x v_2^y)}{(v_1^x)^2 + (v_2^x)^2 - (v_1^y)^2 - (v_2^y)^2} \\ &= -\frac{2\vec{v}^x \cdot \vec{v}^y}{|\vec{v}^x|^2 - |\vec{v}^y|^2}, \end{aligned}$$

one obtains the “minimal” Weyl Hamiltonian (3). In terms of the original velocities, the minimal set of effective parameters (the velocities $\mathbf{w}_0 = (w_{0x}, w_{0y})$, w_x and w_y) reads

$$\begin{aligned} w_{0x} &= v_0^x \cos \vartheta - v_0^y \sin \vartheta, & w_{0y} &= v_0^x \sin \vartheta + v_0^y \cos \vartheta, \\ w_x^2 &= \frac{(v_1^x)^2 + (v_2^x)^2 + (v_1^y)^2 + (v_2^y)^2}{2} + \sqrt{\left[\frac{(v_1^x)^2 + (v_2^x)^2 - (v_1^y)^2 - (v_2^y)^2}{2}\right]^2 + (v_1^x v_1^y + v_2^x v_2^y)^2}, \\ w_y^2 &= \frac{(v_1^x)^2 + (v_2^x)^2 + (v_1^y)^2 + (v_2^y)^2}{2} - \sqrt{\left[\frac{(v_1^x)^2 + (v_2^x)^2 - (v_1^y)^2 - (v_2^y)^2}{2}\right]^2 + (v_1^x v_1^y + v_2^x v_2^y)^2}. \end{aligned} \quad (\text{A3})$$

APPENDIX B: TRANSFORMATION OF THE WEYL HAMILTONIAN UNDER SPACE INVERSION

The ingredients which intervene in the Peierls substitution (9), $\mathbf{q} \rightarrow -i\nabla + e\mathbf{A}(\mathbf{r})$, are vectors, which trans-

form as $\mathbf{V} \rightarrow -\mathbf{V}$ under space inversion. Because of

this transformation property and because the generalized Weyl Hamiltonian (1) is linear in the momentum, we have

$$H_B(\mathbf{r}, \nabla) = -H_B(-\mathbf{r}, -\nabla), \quad (\text{B1})$$

in space representation, where H_B is given in Eq. (11). We now consider a solution of the Schrödinger equation,

$$H_B(\mathbf{r}, \nabla)\psi_\epsilon(\mathbf{r}) = \epsilon\psi_\epsilon(\mathbf{r}),$$

of energy ϵ . Due to the property (B1) under space inversion, one finds that

$$H_B(\mathbf{r}, \nabla)\psi_\epsilon(-\mathbf{r}) = -H_B(-\mathbf{r}, -\nabla)\psi_\epsilon(-\mathbf{r}) = -\epsilon\psi_\epsilon(-\mathbf{r}). \quad (\text{B2})$$

This means that $\psi_\epsilon(-\mathbf{r})$ is a solution of the Schrödinger equation with energy $-\epsilon$, and to each energy ϵ in the upper energy band there exists one at $-\epsilon$ in the lower one. The resulting Landau level energy spectrum is, therefore, symmetric around zero energy.

Notice, however, that this argument is only valid for the generalized Weyl Hamiltonian if one neglects the underlying lattice model for which the Weyl Hamiltonian describes the low-energy properties. As mentioned in the text, Dirac points occur in pairs at non-zero wave vectors, and one thus obtains a twofold valley degeneracy $\xi = \pm 1$. In this case, there is a relative minus sign between the two copies of the Weyl Hamiltonian ξH_B . Space inversion, therefore, becomes an exact symmetry of the model and involves both valleys.

APPENDIX C: ZERO-ENERGY LANDAU LEVEL FOR THE CASE WITH TILT

In this appendix, we show that there exists a zero energy mode for the Hamiltonian H_B (11). We may repre-

sent the ladder operators a and a^\dagger as

$$ae^{i\varphi} = \partial_x + x, \quad a^\dagger e^{-i\varphi} = -\partial_x + x,$$

which act on states described as functions of the real variable x . The latter is not necessarily identical to the x - or x' -variable in the plane, but should rather be viewed as an auxiliary variable that allows for a formal solution of the zero-energy problem.

The Hamiltonian (11), thus, reads

$$H_B = \frac{\sqrt{2w_x w_y}}{l_B} \begin{pmatrix} \tilde{w}_0 x & (x + \partial_x)e^{-i\varphi} \\ (x - \partial_x)e^{i\varphi} & \tilde{w}_0 x \end{pmatrix}, \quad (\text{C1})$$

and we may search the solutions of the zero-energy eigenvalue equation, $H_B\psi_0(x) = 0$, with the ansatz

$$\psi_0(x) = \begin{pmatrix} \alpha \\ \beta \end{pmatrix} e^{-\gamma x^2/2}.$$

This yields the system of linear equations

$$\begin{aligned} \tilde{w}_0 \alpha + e^{-i\varphi}(1 - \gamma)\beta &= 0 \\ e^{i\varphi}(1 + \gamma)\alpha + \tilde{w}_0 \beta &= 0, \end{aligned}$$

which has a non-zero solution if we choose

$$\gamma = \sqrt{1 - \tilde{w}_0^2}. \quad (\text{C2})$$

and, thus,

$$\alpha = -\frac{\tilde{w}_0 e^{-i\varphi}}{1 + \gamma} \beta.$$

Notice that we only obtain bound states, i.e. states that decay at large values of x , for $\tilde{w}_0 < 1$ ($\gamma > 0$ and real), which corresponds to the maximal-tilt condition (5).

-
- ¹ K. S. Novoselov, A. K. Geim, S. V. Morosov, D. Jiang, M. I. Katsnelson, I. V. Grigorieva, S. V. Dubonos, and A. A. Firsov, *Nature* **438**, 197 (2005).
- ² Y. Zhang, Y.-W. Tan, H. L. Stormer, and P. Kim, *Nature* **438** 201, (2005).
- ³ For a recent review, see A. H. Castro Neto, N. M. R. Peres, K. S. Novoselov, and A. K. Geim, arXiv:0709.1163.
- ⁴ S. Katayama, A. Kobayashi, and Y. Suzumura, *J. Phys. Soc. Jpn.* **75**, 054705 (2006).
- ⁵ A. Kobayashi, S. Katayama, Y. Suzumura, and H. Fukuyama, *J. Phys. Soc. Jpn.* **76**, 034711 (2007).
- ⁶ H. Fukuyama, *J. Phys. Soc. Jpn.* **76**, 043711 (2007).
- ⁷ K. Kajita, T. Ojio, H. Fujii, Y. Nishio, H. Kobayashi, A. Kobayashi, and R. Kato, *J. Phys. Soc. Jpn.* **61**, 23 (1992).
- ⁸ N. Tajima, S. Sugawara, M. Tamura, Y. Nishio, and K. Kajita, *J. Phys. Soc. Jpn.* **75**, 051010 (2006).
- ⁹ C. Hotta, *J. Phys. Soc. Jpn.* **72**, 840 (2003).
- ¹⁰ T. Mori, H. Mori, and S. Tanaka, *Bull. Chem. Soc. Jpn.* **72**, 179 (1999).
- ¹¹ R. Kondo, S. Kagoshima, and J. Harada, *Rev. Sci. Instrum.* **76**, 093902 (2005).
- ¹² L. Pauling, *PNAS* **56** 1646 (1966).
- ¹³ S.-L. Zhu, B. Wang, and L.-M. Duan, *Phys. Rev. Lett.* **98**, 260402 (2007).
- ¹⁴ L. Onsager, *Phil. Mag.* **43**, 1006 (1952), I.M. Lifshitz and A.M. Kosevich, *Sov. Phys. J.E.T.P.* **2**, 636 (1956).
- ¹⁵ G. P. Mikitik and Yu. V. Sharlai, *Phys. Rev. Lett.* **82**, 2147 (1999).
- ¹⁶ P. Dietl, F. Piéchon, and G. Montambaux, *Phys. Rev. Lett.* **100**, 236405 (2008).
- ¹⁷ R. Saito, G. Dresselhaus, and M. Dresselhaus, *Physical Properties of Carbon Nanotubes* (Imperial College Press, London, 1998).
- ¹⁸ R. O. Dillon, I. L. Spain, and J. W. McClure, *J. Phys. Chem. Sol.* **38**, 635 (1977).
- ¹⁹ W. A. Harrison, *Phys. Rev. B* **24**, 5835 (1981).
- ²⁰ J.-C. Charlier, J.-P. Michenaud, X. Gonze, and J.-P. Vigneron, *Phys. Rev. B.* **44**, 13237 (1991).

- ²¹ J.-N. Fuchs, M. O. Goerbig, G. Montambaux, and F. Piéchon, *in preparation*.
- ²² N. M. R. Peres, F. Guinea, and A. H. Castro Neto, Phys. Rev. B **73**, 245426 (2006).
- ²³ L. Salem, *Molecular orbital theory of conjugated systems* (W.A. Benjamin, 1966), pages 141-143.
- ²⁴ B. Reulet, A. Yu. Kasumov, M. Kociak, R. Deblock, I. I. Khodos, Yu. B. Gorbatov, V. T. Volkov, C. Journet, and H. Bouchiat, Phys. Rev. Lett. **85**, 2829 (2000).
- ²⁵ M. Huang, H. Yan, D. Song, C. Chen, T. Heinz, J. Hone, (*unpublished*).
- ²⁶ S. Söderholm, P. R. Varekamp, and D. Schweitzer, Phys. Rev. B **52**, 9629 (1995).
- ²⁷ For a review, see e.g. S. Das Sarma and A. Pinczuk, eds., *Perspectives in Quantum Hall Effects*, Wiley, New York (1997).
- ²⁸ E. E. Laukhina, V. A. Merzhanov, S. I. Pesotskii, A. G. Khomenko, E. B. Yagnbskii, J. Ulanski, M. Kryszewski, and J. K. Jeszka, Synth. Met. **70** 797 (1995).
- ²⁹ K. S. Novoselov, D. Jiang, T. Booth, V. V. Khotkevich, S. M. Morozov, A. K. Geim, PNAS **102**, 10451 (2005)
- ³⁰ M. L. Sadowski, G. Martinez, M. Potemski, C. Berger, and W. A. de Heer, Phys. Rev. Lett. **97**, 266405 (2006); for corrections to the \sqrt{Bn} scaling at larger energies, see P. Plochocka, C. Faugeras, M. Orlita, M. L. Sadowski, G. Martinez, M. Potemski, M. O. Goerbig, J.-N. Fuchs, C. Berger, and W. A. de Heer, Phys. Rev. Lett. **100**, 087401 (2008).
- ³¹ Z. Jiang, E. A. Henriksen, L. C. Tung, Y.-J. Wang, M. E. Schwartz, M. Y. Han, P. Kim, and H. L. Stormer, Phys. Rev. Lett. **98**, 197403 (2007).